

Kosterlitz-Thouless transition of quantum XY model in two dimensions

Kenji HARADA and Naoki KAWASHIMA¹

Division of Applied Systems Science, Kyoto University, Sakyo-ku, Kyoto 606-01

¹ *Department of Physics, Toho University, Miyama 2-2-1, Funabashi 274, Japan*

(Received March 2, 1998)

The two-dimensional $S = 1/2$ XY model is investigated with an extensive quantum Monte Carlo simulation. The helicity modulus is precisely estimated through a continuous-time loop algorithm for systems up to 128×128 near and below the critical temperature. The critical temperature is estimated as $T_{KT} = 0.3427(2)J$. The obtained estimates for the helicity modulus are well fitted by a scaling form derived from the Kosterlitz renormalization group equation. The validity of the Kosterlitz-Thouless theory for this model is confirmed.

KEYWORDS: Quantum XY model, Kosterlitz-Thouless transition, quantum Monte Carlo, helicity modulus

§1. Introduction

The XY model in two dimensions has been discussed in various contexts such as magnets with easy-plane anisotropy, superconductivity in a thin layer, granular superconducting materials, and insulator-superfluid transition in He^4 systems. Naturally, a number of works were devoted to clarifying the nature of the phase transition and the low-temperature phase of this model. Among them notable was a large scale Monte Carlo simulation by Ding and Makivć.^{1,2)} Based on computation of the linear in-plane susceptibility and the correlation length at various temperatures, they concluded that a phase transition takes place at $T_{KT} = 0.350(4)$ ^{1,2)} or $0.353(3)$,³⁾ and that this transition is of Kosterlitz-Thouless (KT)⁴⁾ type. However, it is technically difficult to distinguish an exponential divergence from an algebraic one. Because of this difficulty, the validity of their conclusion on the nature of the phase transition was questioned.^{5,6)} For the same reason, in spite of their very extensive Monte Carlo calculation, Gupta and Baillie^{7,8)} did not withdraw a definitive conclusion although their numerical results seemed to suggest that the phase transition of the classical XY model is exactly what the KT theory predicts.

It should be noted that the above-mentioned technical difficulty is partially due to the absence of finite-size-scaling type analysis which is a common and powerful tool in most numerical studies. However, Solym and Ziman⁹⁾ pointed out that the straightforward application of the ordinary finite-size-scaling analysis leads to a wrong result not only when the power-law temperature dependence of the correlation length, which is wrong, is assumed but also when the correct exponential divergence is assumed. They studied the size dependence of the first excitation gap in the $S = 1/2$ anisotropic XXZ model in one dimension, which is exactly solvable and known to have a transition of the KT type at the anti-ferromagnetic isotropic point. They found that the exact estimates for the finite systems do not fit into the standard form of the finite-size-scaling at the critical point.

Therefore, to obtain a definitive answer to the question concerning the nature of the phase transition, we need to have a correct form for the system size dependence of quantities of interest. In previous studies, to our knowledge, a systematic study of such system size dependence has been missing for the quantum XY model. There are, however, some reports on classical XY models. Instead of using the ordinary finite-size-scaling form, Weber and Minnhagen¹⁰⁾ used the Kosterlitz renormalization group equation¹¹⁾ for the data analysis in their study of the classical XY model in two dimensions. They verified the KT type phase transition by comparing the size dependence of the helicity modulus, Υ , at the critical temperature with the renormalization group flow along the critical line that converges to the KT fixed point with a logarithmically slow convergence. They observed not only that the computed helicity modulus exhibits the logarithmic dependence on the length scale but also that even the pre-factor of this logarithmic term agreed with the predicted one. Following the same idea, Olsson¹²⁾ performed a more detailed analysis of the classical model with an extensive Monte Carlo simulation. He observed that the system-size dependence of the helicity modulus agreed with the form derived from the Kosterlitz renormalization group equation below and above the critical temperature as well as right at the critical temperature.

The helicity modulus is known to exhibit the universal jump at the critical temperature.¹³⁾ This quantity corresponds to the super-fluid density when the model is regarded as a Boson system with hard-cores. In the world-line quantum Monte Carlo method,¹⁴⁾ the helicity modulus is represented as the fluctuation in the total winding number of world-lines by the following equation,¹⁵⁾

$$\Upsilon = (T/2)\langle \mathbf{W}^2 \rangle, \quad (1)$$

where $\mathbf{W} \equiv (W_x, W_y)$ with W_x (W_y) being the total winding number in the x (y) direction. It is difficult to measure this quantity by means of a conventional world-line quantum Monte Carlo method because a conven-

tional algorithm is not ergodic in that the winding number is not allowed to vary. In principle, it is possible to make it ergodic by introducing additional global movements of world-lines. In practice, however, such additional and in most cases “ad-hoc” global movements are seldom accepted and the resulting estimates of the helicity modulus have large statistical errors. Therefore, Makivić¹⁶⁾ divided the whole system into a number of sub-systems and measured the winding number for each sub-system which may vary. It is not totally clear if this alternative way of measurement gives the same answer as the conventional one does. Another difficulty of the conventional Monte Carlo method is its long auto-correlation time near and below the critical temperature. These difficulties limited the accuracy and the precision of the Makivić’s estimates of the helicity modulus and narrowed the accessible temperature range of simulation.

In the present paper, we report some results of the quantum Monte Carlo simulation of the $S = 1/2$ XY model using the loop algorithm^{17,18,19)} with both discrete and continuous imaginary time representations.²⁰⁾ Similar results for smaller systems with discrete imaginary time representation have been reported elsewhere.²¹⁾ The use of the loop algorithm eliminates both of the above-mentioned difficulties. There the number of particles as well as the winding number can vary. At the same time, there are a number of reports^{18,19)} on the drastic improvement in the auto-correlation time of the simulation by loop algorithms. We aim at a detailed and precise comparison between the quantum XY model and the theory by Kosterlitz¹¹⁾ through an accurate estimation of the thermal fluctuation in the winding number near and below the critical temperature. We show that such an estimation allows us to examine a new scaling form different from the ordinary finite-size-scaling. In this scaling form, the distance from the critical point, i.e., $K - K_{KT}$ appears in the form of $(K - K_{KT})(\log(L/L_0))^2$, in contrast to $(K - K_{KT})L^{y_T}$ in the ordinary finite-size-scaling. At the same time, the quantity $x \equiv \langle (\pi/2)\mathbf{W}^2 \rangle - 2$ scales as $x \log(L/L_0)$ rather than x/L^ω with some exponent ω . This “scaling” form is consistent with Olsson’s fitting functions.

In § 2, we describe loop algorithms on discrete and continuous imaginary time. In § 3, the definition of helicity modulus, its improved estimator and details of simulations are described. In § 4, estimates of the helicity modulus are presented and we summarize the results in § 5.

§2. Monte Carlo Algorithms

2.1 World-line Monte Carlo method for quantum XY model

The $S = 1/2$ quantum XY model is defined by the following Hamiltonian.

$$\hat{H} = \sum_{\langle \mathbf{i} \mathbf{j} \rangle} \hat{H}_{\mathbf{i} \mathbf{j}} = -J \sum_{\langle \mathbf{i} \mathbf{j} \rangle} (\hat{S}_{\mathbf{i}}^x \hat{S}_{\mathbf{j}}^x + \hat{S}_{\mathbf{i}}^y \hat{S}_{\mathbf{j}}^y), \quad (2)$$

where $\langle \mathbf{i} \mathbf{j} \rangle$ runs over all nearest-neighbor pairs on a square lattice. As for the spin operators, we use the convention in which $(\hat{S}_{\mathbf{i}}^\mu)^2 = 1/4$ ($\mu = x, y, z$). We will

take J as the unit of the energy scale in what follows.

In world-line Monte Carlo methods for d dimensional quantum systems, we generate world-line configurations in the $(d+1)$ dimensional space-time with probability density proportional to the integrand of the Feynmann path integral. In a conventional quantum Monte Carlo simulation, it is customary to discretize the imaginary time in the path integral form to derive a model with classical degrees of freedom in $(d+1)$ dimensions. We then perform an ordinary Metropolis-type Monte Carlo simulation of this classical system. This standard procedure is called Suzuki-Trotter (ST) decomposition.¹⁴⁾ Due to the recent development of the continuous time representation,²⁰⁾ it is no longer necessary to discretize the imaginary time by the ST decomposition. Nevertheless, we start with it because it is still the most natural way to explain the algorithm. In the actual computation, we have used both of the discrete and continuous time algorithms.

Our Hamiltonian can be considered as a sum of four sub-Hamiltonians: $\hat{H} = \hat{H}_A + \hat{H}_B + \hat{H}_C + \hat{H}_D$. Each sub-Hamiltonian is a sum of operators commutable with each other, i.e.,

$$\hat{H}_X = \sum_{\langle \mathbf{i} \mathbf{j} \rangle \in X} \hat{H}_{\mathbf{i} \mathbf{j}} \quad (X = A, B, C, D) \quad (3)$$

where

$$A \equiv \{ \langle \mathbf{i} \mathbf{j} \rangle | \mathbf{i} \in \text{odd column}, \mathbf{j} = \mathbf{i} + \mathbf{e}_x \}, \quad (4)$$

$$B \equiv \{ \langle \mathbf{i} \mathbf{j} \rangle | \mathbf{i} \in \text{odd row}, \mathbf{j} = \mathbf{i} + \mathbf{e}_y \}, \quad (5)$$

$$C \equiv \{ \langle \mathbf{i} \mathbf{j} \rangle | \mathbf{i} \in \text{even column}, \mathbf{j} = \mathbf{i} + \mathbf{e}_x \}, \quad (6)$$

$$D \equiv \{ \langle \mathbf{i} \mathbf{j} \rangle | \mathbf{i} \in \text{even row}, \mathbf{j} = \mathbf{i} + \mathbf{e}_y \}, \quad (7)$$

and \mathbf{e}_x (or \mathbf{e}_y) is a unit lattice vector in the x (or y) direction.

Using the ST decomposition, we transform the partition function into the following form,

$$Z \approx \sum_S \prod_p w(S_p). \quad (8)$$

Here, p stands for a plaquette in the $(d+1)$ dimensional space-time with two edges perpendicular and the other two parallel to the imaginary time axis. The space-time location of its left-bottom corner is given by (\mathbf{i}, t) with

$$t \equiv \begin{cases} (4n)\Delta\tau & \text{if } \mathbf{i} \in A \\ (4n+1)\Delta\tau & \text{if } \mathbf{i} \in B \\ (4n+2)\Delta\tau & \text{if } \mathbf{i} \in C \\ (4n+3)\Delta\tau & \text{if } \mathbf{i} \in D \end{cases}, \quad (9)$$

where the imaginary time spacing, $\Delta\tau \equiv \beta/m$, is the unit of the discretization of the imaginary time. The number of steps m is called the Trotter number. The symbol S_p in eq. (8) is the local spin configuration on a plaquette p and $w(S_p)$ is the two-spin propagator defined below. The symbol S in eq. (8) stands for the spin configuration of the whole space-time or the union of all S_p ’s, i.e., $S \equiv \bigcup_p S_p$. We denote the four states of spin pairs by $1 = \uparrow\uparrow$, $2 = \uparrow\downarrow$, $3 = \downarrow\uparrow$ and $4 = \downarrow\downarrow$. Then, the two-spin

propagator can be written explicitly as

$$w(S_p) \equiv \left\langle S_p^{(\text{final})} \left| \exp \left(-(\Delta\tau) \hat{H}_{ij} \right) \right| S_p^{(\text{initial})} \right\rangle$$

$$= \begin{pmatrix} 1 & 0 & 0 & 0 \\ 0 & \cosh\left(\frac{\Delta\tau J}{2}\right) & \sinh\left(\frac{\Delta\tau J}{2}\right) & 0 \\ 0 & \sinh\left(\frac{\Delta\tau J}{2}\right) & \cosh\left(\frac{\Delta\tau J}{2}\right) & 0 \\ 0 & 0 & 0 & 1 \end{pmatrix}. \quad (10)$$

The symbol $S_p^{(\text{initial})}$ and $S_p^{(\text{final})}$ stand for the local state of two corners at the bottom and top edges of the plaquette p , respectively. The local state of the whole plaquette, S_p , can be regarded as the combination of the two. In the 4×4 matrix representation of eq. (10), the column index corresponds to four possible initial state, $S_p^{(\text{initial})}$, and the row index $S_p^{(\text{final})}$.

2.2 Loop algorithm with discrete imaginary time

In a loop algorithm, we first assign a graph G_p to each plaquette. A graph specifies the set of local states from which new state S'_p is chosen. In other words, G_p imposes a restriction on the local state. We call it a “graph” because such a restriction can be conveniently expressed pictorially by drawing a line connecting two sites whose relative orientation is not allowed to be changed under the restriction G_p . A group of spins connected by a sequence of such lines is called a cluster. In the present case each site is shared by two plaquettes and it is connected to another site in each of the two plaquettes. Therefore, a cluster is a loop in the present case. Hence the name of the algorithm. In general, however, we need to introduce branching or connecting more than two sites in a plaquette. For example, in the case of the Ising-like XXZ model, we need to include a graph in which all four corners are connected. Once we assign graphs to all plaquettes, we change the spin variables by regarding each cluster as a block spin and flipping it with an appropriate probability. In what follows, we briefly describe how we should choose the probability for assigning a graph to each plaquette and the probability for changing the spin variables.

First, the two-spin propagator or the local Boltzmann weight $w(S_p)$ can be written as

$$w(S_p) = \sum_{G_p} w(S_p, G_p),$$

$$w(S_p, G_p) \equiv v(G_p) \Delta(S_p, G_p). \quad (11)$$

Here the function $\Delta(S_p, G_p)$ takes on the value 1 when S_p is compatible with the graph G_p , and it takes the value 0, otherwise.

For the $S = 1/2$ quantum XY model, the graph weight, $v(G_p)$, is defined in Table I. The summation in eq. (11) is taken over the three graphs depicted in Fig. 1. We represent $\Delta(S_p, G_p)$ by the matrices in the same manner as eq. (10):

$$\Delta(\cdot, 1) = \begin{pmatrix} 1 & 0 & 0 & 0 \\ 0 & 1 & 0 & 0 \\ 0 & 0 & 1 & 0 \\ 0 & 0 & 0 & 1 \end{pmatrix}, \Delta(\cdot, 2) = \begin{pmatrix} 0 & 0 & 0 & 0 \\ 0 & 1 & 1 & 0 \\ 0 & 1 & 1 & 0 \\ 0 & 0 & 0 & 0 \end{pmatrix}$$

$$\Delta(\cdot, 3) = \begin{pmatrix} 1 & 0 & 0 & 0 \\ 0 & 0 & 1 & 0 \\ 0 & 1 & 0 & 0 \\ 0 & 0 & 0 & 1 \end{pmatrix}. \quad (12)$$

A Markov process generated by a traditional world-line algorithm stays in the spin configuration space:

$$S^{(1)} \rightarrow S^{(2)} \rightarrow S^{(3)} \rightarrow \dots, \quad (13)$$

whereas a Markov process of a loop algorithm alternates between the spin and graph configuration spaces:

$$S^{(1)} \rightarrow G^{(1)} \rightarrow S^{(2)} \rightarrow G^{(2)} \rightarrow S^{(3)} \rightarrow G^{(3)} \rightarrow \dots \quad (14)$$

The transition probabilities between the spin and graph configurations are defined as follows:

$$P(S \rightarrow G) \equiv \frac{\prod_p w(S_p, G_p)}{\sum_{G'_p} \prod_p w(S_p, G'_p)}, \quad (15)$$

$$P(G \rightarrow S) \equiv \frac{\prod_p w(S_p, G_p)}{\sum_{S'_p} \prod_p w(S'_p, G_p)}, \quad (16)$$

where $G \equiv \bigcup_p G_p$ is the global graph. It is easy to check that these transition probabilities satisfy the detailed balance.

We see from eq. (16) that $P(G \rightarrow S)$ is vanishing if S_p is not compatible to G_p for any p , while it takes on a value independent of S as long as all S_p ’s are compatible to G_p ’s. This means that sites belonging to the same loop should be flipped simultaneously with a probability $1/2$, and two distinct loops should be flipped independently. Since flipping a loop is a global update, one may imagine that the cluster algorithm reduces the autocorrelation time due to slow relaxation modes associated with large structures. This is indeed the case as reported in a number of articles.^{18, 19}

2.3 Loop algorithm with continuous imaginary time

Beard and Wiese²⁰⁾ pointed out that we can take the continuous imaginary time limit ($\Delta\tau \rightarrow 0$) of the above-mentioned algorithm to obtain another algorithm which works directly on continuous time, instead of computing quantities using discrete time with various $\Delta\tau$ ’s and extrapolating the results to get estimates in the continuous time limit. In the discrete time version, we need to be careful in decomposing the Boltzmann operator in order to keep the correction term of high order in $\Delta\tau$. This is why we have to split the Hamiltonian into several pieces as we did in previous sections (eq. (3)). In deriving the continuous time version, however, we can avoid this complication because any correction term vanishes in the continuous time limit. In other words, we have to keep only the lowest order term to get the correct algorithm. This fact makes the derivation of the algorithm a little simpler as we see below.

The matrix elements of the partial Hamiltonian \hat{H}_{ij} can be directly represented by a graph variable G_p as

$$\langle S_p^{(\text{final})} | \hat{H}_{ij} | S_p^{(\text{initial})} \rangle \equiv - \sum_{G_p} a(G_p) \Delta(S_p, G_p). \quad (17)$$

(For the $S = 1/2$ quantum XY model, the $a(G_p)$ is

defined in Table I). Then, for small $\Delta\tau$, the weights $w(S_p)$ are expressed, up to the lowest order, as

$$w(S_p) \approx I(S_p) + \Delta\tau \sum_{G_p} a(G_p) \Delta(S_p, G_p), \quad (18)$$

where $I(S_p)$ is the matrix element of the identity operator on a plaquette with a “height” $\Delta\tau$ in the imaginary time direction. For simplicity, we set $\Delta(S_p, 1) \equiv I(S_p)$ in the following. Taking the limit of an infinitesimal imaginary time spacing ($\Delta\tau \rightarrow 0$), transition probabilities (eq. (15)) on a plaquette are reduced to the followings:

1. If the present state S_p is compatible to the graph $G_p = 1$, i.e., if there is no exchange of spins in the time interval $(t, t + \Delta\tau)$,

$$P(S_p \rightarrow G_p) = (\Delta\tau) a(G_p) \Delta(S_p, G_p) \quad (G_p \neq 1),$$

$$P(S_p \rightarrow 1) = 1 - \sum_{G'_p \neq 1} P(S_p \rightarrow G'_p). \quad (19)$$

2. If the present state S_p is incompatible to the graph $G_p = 1$, i.e., if the state at t is different from that at $t + \Delta\tau$,

$$P(S_p \rightarrow G_p) = \frac{a(G_p) \Delta(S_p, G_p)}{\sum_{G'_p \neq 1} a(G'_p) \Delta(S_p, G'_p)} \quad (G_p \neq 1),$$

$$P(S_p \rightarrow 1) = 0 \quad (20)$$

We apply eq. (19) to plaquettes (with infinitesimal “heights”) at which world-lines continue along the Trotter direction. The probability of choosing a graph $G_p \neq 1$ in the imaginary time interval $\Delta\tau$ is $(\Delta\tau) a(G_p) \Delta(S_p, G_p)$. This means that in the continuous limit we distribute graphs G_p over such an interval uniformly, i.e., with a Poisson process, with the probability density $a(G_p) \Delta(S_p, G_p)$. On the other hand, eq. (20) gives the probability (not probability density) with which a graph is assigned to each point of time where the local state is changed or two neighboring world-lines are exchanged.

Consequently, for general models, the loop algorithm with continuous imaginary time can be summarized as follows. For each pair of nearest neighbor world-lines,

1. distribute graphs $G_p (\neq 1)$ with a Poisson process with eq. (19) over every imaginary time interval in which world-lines are not interrupted,
2. choose a graph G_p with eq. (20) at each point of time where states are exchanged between the two sites,
3. assign the graph $G_p = 1$ elsewhere,

and then update spin values by flipping clusters (eq. (16)). To restate this procedure for the specific case of $S = 1/2$ quantum XY model,

1. for each uninterrupted time interval during which spins on these world-lines are antiparallel, generate “horizontal reconnections” (graph $G_p = 2$ in Fig. 1) of world-lines with probability density $J/4$, and for parallel spins, generate “diagonal reconnections” (graph $G_p = 3$) of world-lines with probability density $J/4$,
2. at each point of time where states are exchanged, assign a horizontal or diagonal reconnection with

equal probability (1/2),

3. assign the graph $G_p = 1$ elsewhere.

§3. Numerical Results

3.1 Helicity modulus

In the present paper, we focus on the helicity modulus because it may be directly related to the solution of the Kosterlitz renormalization group equation and therefore may exhibit some behavior characteristic of the KT transition. We have measured the helicity modulus by computing the fluctuation in the total winding number of world-lines with eq. (1). The total winding number W_x (or W_y) is defined as the sum of winding numbers of individual world-lines. The winding number of an individual world-line is the number of times the world-line wraps around the system in the x or y direction before coming back to its starting point. The total winding number of world-lines for up spins is exactly the same in magnitude as that for down spins and has the opposite sign. We here count only the winding numbers for up spins. Alternatively, W_x can be defined as

$$W_x = \frac{1}{L_x} \sum_p \alpha_x(S_p),$$

$$\frac{1}{L_x} \alpha_x(S_p) \equiv \sum_{\mathbf{i} \in p} c_{\mathbf{i}}^x S_{\mathbf{i}}^z, \quad (21)$$

where L_x is the lattice size in the x direction. The symbol $\alpha_x(S_p)$ stands for the function which takes on the value 1 (or -1) if an up-spin world-line passes through the plaquette p in the positive (or negative) x direction and takes on the value 0, otherwise. Equivalently, $c_{\mathbf{i}}^x$ is a constant which only depends on site \mathbf{i} and takes on the value $\pm 1/(4L_x)$ or zero. The other winding number W_y can be also calculated in the same manner.

3.2 Improved estimator of helicity modulus

In cluster type algorithms, it is often advantageous to re-express physical quantities in terms of graph variables rather than spin variables. The best known example is the graphical estimator for the linear magnetic susceptibility in the Swendsen–Wang algorithm for the uniform Ising model where the susceptibility is measured as the average cluster size rather than as the second moment of the sum of all spin variables. For the winding number, too, we can use a similar improved estimator. In our simulation, we have used this improved estimator for the squared winding number of world-lines. Equation (21) defines the ordinary estimator in terms of spin variables and it can be rewritten as

$$\mathbf{W}^2 = W_x^2 + W_y^2, \quad (22)$$

$$W_x \equiv \sum_{\mathbf{i}} c_{\mathbf{i}}^x S_{\mathbf{i}}^z, \quad W_y \equiv \sum_{\mathbf{i}} c_{\mathbf{i}}^y S_{\mathbf{i}}^z, \quad (23)$$

where $c_{\mathbf{i}}^x$ and $c_{\mathbf{i}}^y$ are constants which only depend on site \mathbf{i} . To be more specific, $c_{\mathbf{i}}^x = 1/4L_x$ when the site \mathbf{i} locates at the lower-left or upper-right corner of a shaded plaquette and $c_{\mathbf{i}}^x = -1/4L_x$ otherwise. (Which is ‘left’ is an irrelevant question here as it is a matter of the overall sign of the winding number and we are interested only

in its squared value).

Here, we should notice that the winding number $W_x^{(l)}$ or $W_y^{(l)}$ of a loop l formed in the process of the graph assignment can be expressed in terms of c_i^x and c_i^y defined above as follows,

$$W_x^{(l)} \equiv 2 \sum_{i \in l} c_i^x S_i^z, \quad W_y^{(l)} \equiv 2 \sum_{i \in l} c_i^y S_i^z. \quad (24)$$

Then, the ordinary estimator \mathcal{O} for the squared winding number can be decomposed into two parts:

$$\mathcal{O} = \mathcal{O}_{impr} + \mathcal{O}_{rem}, \quad (25)$$

where \mathcal{O}_{impr} and \mathcal{O}_{rem} are defined as

$$\mathcal{O}_{impr} = \frac{1}{4} \left(\sum_l W_x^{(l)}{}^2 + \sum_l W_y^{(l)}{}^2 \right), \quad (26)$$

$$\mathcal{O}_{rem} = \frac{1}{4} \left(\sum_{l \neq l'} W_x^{(l)} W_x^{(l')} + \sum_{l \neq l'} W_y^{(l)} W_y^{(l')} \right). \quad (27)$$

Since loops are flipped independently, the expectation values of all the cross terms in \mathcal{O}_{rem} are vanishing. Therefore,

$$\langle \mathcal{O}_{rem} \rangle = 0. \quad (28)$$

For the same reason, we can derive another useful equation,

$$\langle \mathcal{O}_{impr} \cdot \mathcal{O}_{rem} \rangle = 0. \quad (29)$$

Equation (28) leads to

$$\langle \mathcal{O} \rangle = \langle \mathcal{O}_{impr} \rangle. \quad (30)$$

This implies that the \mathcal{O}_{impr} is another estimator of the squared winding number. The new estimator \mathcal{O}_{impr} depends only on the graph variables. We can see that this new estimator is really “improved” as follows.

Intuitively, one graph configuration represents 2^{N_l} spin configurations, where the N_l is the number of loops in the system. Therefore, a sampling of \mathcal{O}_{impr} corresponds to taking an averaged value over many samplings of \mathcal{O} . From eq. (29), the variance of \mathcal{O} is related to those of \mathcal{O}_{impr} and \mathcal{O}_{rem} as

$$\text{Var}(\mathcal{O}) = \langle (\mathcal{O}_{impr} + \mathcal{O}_{rem})^2 \rangle - \langle \mathcal{O}_{impr} + \mathcal{O}_{rem} \rangle^2 \quad (31)$$

$$= \text{Var}(\mathcal{O}_{impr}) + \text{Var}(\mathcal{O}_{rem}) \quad (32)$$

$$\geq \text{Var}(\mathcal{O}_{impr}). \quad (33)$$

Equation (33) is valid for other improved estimators of the observable such as the one for the susceptibility or structure factor. Although we have introduced the improved estimator based on the discrete time representation, we can use the same definition in the continuous time representation as well.

We compared the error between two estimators in long runs at various temperatures. We found that the new estimator reduces errors in about twenty per cent and the total performance of the new estimator is about 1.5 times better than that of the conventional one in terms of the computational time required.

3.3 Simulations

In what follows, we present numerical results both from our older set of simulations performed with a discrete time version of the code and from our newer set with a continuous time version. We have taken various temperatures between 0.22 and 0.60 and used lattices with $L = 8, 12, 16, 24, 32, 48, 64, 96$ and 128 in our simulation. For simulations with the discrete time version, we have used $m = 8, 16$ and 32 for the Trotter number. When the systematic error of Trotter discretization exceeds the statistical error, we have reduced the systematic error by the extrapolation to $m = \infty$ using three different Trotter numbers. For $L = 12, 24, 48, 96$ and 128 at all temperatures and for all L 's near the critical temperature, we have used the continuous time version.

The length of a typical run on $L = 128$ at each temperature is more than 10^6 Monte Carlo sweeps (MCS). The most time-consuming part in the entire code is the cluster identification. It is a task of assigning each spin a number that specifies which cluster the spin belongs to. In doing this, we only use the information of the local connectivity. To make a good use of vector processors for this kind of task, we need to use a vectorizable algorithm. For the discrete version of the code, we adopted an efficient vectorized code following Mino's idea.²²⁾ This idea is based on the “divide-and-conquer” strategy. In this strategy, we firstly divide the lattice into many small sub-lattices and identifies clusters in each sub-lattice neglecting the connectivity outside of the cluster. This process can be easily vectorized or parallelized because cluster identifications of different sub-lattices are independent of each other. We then combine two adjacent original sub-lattices to form a larger sub-lattice and identify clusters in this sub-lattice. In doing this, we can use the information of the clusters in the smaller sub-lattices which have already been obtained in the previous step. We repeat this procedure until all the sub-lattices are combined into a single lattice, i.e., the original whole lattice. Using this algorithm, we achieved the efficiency of 1.5 million site updates per second per one vector processor on Fujitsu VPP500. For the loop algorithm on continuous imaginary time, we used a parallel computer and took trivial parallel approach. Our code does about $29000/(L^2\beta)$ sweeps per second on a node of Hitachi SR2201.

In our simulations, each run is divided into several bins. The length of a bin is taken large enough so that bin averages may be statistically independent from each other at least approximately. In order to check this condition, we have measured autocorrelation times of the improved estimator of the squared winding number at low temperatures $T < 0.35J$ by the standard binning analysis for a run of 10^5 MCS with $L = 64$. They turned out to be smaller than 2 MCS in all cases. We have not observed any difficulty due to low temperature except that, trivially, the computational time per one Monte Carlo step increases proportional to the inverse temperature. The statistical independence among bins is assured, because the smallest bin length used is 1000 MCS. An error bar shown in the figures in the present paper represents one standard deviation. Results of the squared winding number $\langle \mathbf{W}^2 \rangle$ are summarized in Table

II.

§4. Universal jump in the helicity modulus

4.1 Kosterlitz renormalization group equations

The helicity modulus can be regarded as the renormalized coupling constant that appears in the Kosterlitz renormalization group equations. Furthermore, Weber and Minnhagen¹⁰⁾ regarded the renormalization group flow of the solution as the system size dependence of the helicity modulus. They observed that the estimated values at the critical temperature agree well with the theoretical prediction derived from this idea. In the present paper, as we see below, we follow their idea but use a different method for the analysis in which not only the data at the critical temperature but also off-critical data are taken into account simultaneously.

The Kosterlitz renormalization group equations are

$$\frac{dx}{dl} = -y^2, \quad \frac{dy}{dl} = -xy. \quad (34)$$

Here, x and y are renormalized parameters after a renormalization operation up to the length scale $L \equiv L_0(T)e^l$ where $L_0(T)$ is some characteristic length of the order of the lattice constant and has no singularity at $T = T_{\text{KT}}$. The renormalized coupling constant x is related to the helicity modulus and the squared winding number by the following equations:¹³⁾

$$x = \frac{\pi \Upsilon}{T} - 2 = \frac{\pi}{2} \langle \mathbf{W}^2 \rangle - 2. \quad (35)$$

Equation (34) has an integral

$$\Delta(T) \equiv x^2(l) - y^2(l), \quad (36)$$

which does not depend on $l \equiv \log(L/L_0(T))$. As a function of T , this integral has no singularity at $T = T_{\text{KT}}$. Therefore we can expand it in terms of the distance from the critical temperature, i.e., $\Delta(K) = a(K - K_{\text{KT}}) + b(K - K_{\text{KT}})^2 + \dots$ where $K \equiv J/T$. The solution of eq. (34) is given by

$$x(T, L) = \begin{cases} \sqrt{|\Delta|} \coth(\sqrt{|\Delta|}l) & (K > K_{\text{KT}}) \\ l^{-1} & (K = K_{\text{KT}}) \\ \sqrt{|\Delta|} \cot(\sqrt{|\Delta|}l) & (K < K_{\text{KT}}). \end{cases} \quad (37)$$

This solution is a special case of the following form:

$$x(T, L) = l^{-1} f(\Delta l^2). \quad (38)$$

This “finite-size-scaling” form can be obtained from the ordinary one

$$x(T, L) = L^\omega g(\Delta L^{1/\nu}) \quad (39)$$

by replacing L by $l = \log(L/L_0(T))$. However, it is easy to see that eq. (38) cannot be made consistent with eq. (39) no matter what values are used for the exponents ω and ν . It should be also pointed out that even if we consider a little more general form for the ordinary finite size scaling

$$x(T, L) = L^\omega g(\xi(T)/L) \quad (40)$$

allowing $\xi(T)$ to have the correct temperature dependence, it is still impossible to cast the solution eq. (37)

into this form.

From the solution eq. (37), it can be seen that the “scaling function” $f(X)$ has no singularity at $X=0$. The scaling function should take on the value 1 at the critical point:

$$f(X) = 1 + O(X). \quad (41)$$

Note also that our scaling form eq. (38) is consistent with Olsson’s fitting function [Equations (11a-c) with (16) and (18) in ref. 12].

4.2 Finite-size-scaling around T_c

In Fig. 2, the squared winding number is plotted against the temperature. We can see the strong system size dependence characteristic to the KT transition especially around and above the critical temperature. Because of this large size dependence it is virtually impossible to estimate the critical temperature and the critical indices without knowing the “scaling form” that describes the system size dependence. Figure 3 shows the same data rescaled using eq. (38). The parameters K_{KT} and L_0 are chosen to minimize the cost function defined in Appendix.

In Fig. 4, the contour plot of the cost function is shown. The cost function is the measure of the “badness” of the scaling plot. It is basically the deviation from the local linear approximation. In order to eliminate data out of critical region, we have to select data points for the analysis. We have eliminated data points outside of the region,

$$\frac{4}{\pi} \leq \langle \mathbf{W}^2 \rangle \leq \frac{4}{\pi} + \frac{1}{2}, \quad (42)$$

$$-1.5 \leq x \equiv (K - K_{\text{KT}})(\log(L/L_0))^2 \leq 1.5. \quad (43)$$

The value of the cost function at the optimal choice of the parameters tends to be smaller as we eliminate more data points away from the critical point, making the resulting estimate more reliable. We have also selected data points with respect to the system size. However, if we eliminate too many data points the cost function does not have a meaningful minimum. As long as we obtain a meaningful minimum, the results do not significantly depend on the minimum system size adopted, as can be seen in Fig. 4. For the upper contour plot in Fig. 4 we have used data for system size $L \geq 8$, whereas for the lower we used $L \geq 12$.

We here quote the estimates adopted in Fig. 3:

$$T_{\text{KT}} = 0.3427(2)J, \quad L_0 = 0.29(2). \quad (44)$$

The minimum value of the cost function turns out to be 1.9. The deviation of this value from unity suggests the presence of correction to scaling. We can see from Fig. 3, that the value of the scaling function $f(x)$ at $x = 0$ is close to unity in agreement with the prediction (eq. (41)). The error in $f(0)$ was determined in a similar fashion to those for T_{KT} and L_0 . It results in

$$f(0) = 1.0(1). \quad (45)$$

This agreement can hardly be explained unless the Kosterlitz-Thouless picture is assumed and is a clear in-

dication for its validity in the present model.

4.3 Finite-size-scaling at T_c

We have also tried another analysis following Weber and Minnhagen,¹⁰⁾ namely, measuring the chi-square values of the fitting to the critical form (The second equation in eq. (37)) as a function of the temperature. To be more specific, we assumed at each temperature the following system size dependence of the helicity modulus.

$$\frac{\pi\Upsilon}{2T} = \frac{\pi}{4}\langle\mathbf{W}^2\rangle = A(T) \left(1 + \frac{1}{2\log(L/L_0(T))}\right) \quad (46)$$

This fitting form is expected to be correct only at the critical point with $A(T_{KT}) = 1$ (eq. (38) and eq. (41)).

Since the number of data at each temperature is not enough, the critical temperature cannot be determined as the one at which the fitting is the best. Instead, we have tried two other procedures. One is to fix $A(T)$ to be 1 (but keep L_0 as a fitting variable) and measure the chi-square values of the fitting. The result is shown in Fig. 5. From this figure we conclude that $T_{KT} = 0.3430(5)$. The other procedure is to allow the coefficient $A(T)$ to vary and see where $A(T)$ crosses the line of $A = 1$, which should be the case at the critical temperature. The estimated coefficient $A(T)$ as a function of temperature while both A and L_0 are allowed to vary is shown in Fig. 6. The critical temperature is estimated by a linear fitting of the data, yielding

$$T_{KT} = 0.34271(5)J, \quad (47)$$

which is consistent with eq. (44).

§5. Conclusion

We have obtained accurate estimates of the helicity modulus as a function of temperature and system size. The results fit into the special finite size scaling form derived from the Kosterlitz renormalization group equation identifying the renormalization scale with the system size. By this scheme we have avoided a technically difficult comparison between an exponential divergence and an algebraic one. The coincidence of the estimated critical value of the scaling function with the predicted one confirms the KT nature of the phase transition. In the numerical simulation we have used loop algorithms in both discrete and continuous time representations. Both of them have turned out to be quite efficient and advantageous especially in estimating the helicity modulus which is usually a conserved quantity in conventional Monte Carlo simulation.

A part of the numerical computation was done using Fujitsu VPP500 at ISSP, the university of Tokyo and Kyoto University Data Processing Center and Hitachi SR2201 at the computer center of the University of Tokyo. N.K.'s work is supported by Grant-in-Aid for scientific research (No. 09740320) from the Ministry of Education, Science and Culture of Japan.

Appendix: Cost function for evaluating finite-size-scaling plots

In this appendix, we present a new estimator for evaluating finite-size-scaling plots. The estimator is basically a deviation from a local linear approximation analogous to the previous estimator.²³⁾ The advantage of this type of approaches is that we do not need to assume any specific functional form for the scaling function. These estimators are functions of trial values for various parameters such as critical indices and temperature; K_{KT} and L_0 in the present case. Since the previous estimator was discontinuous as a function of these parameters, searching for its minimum — the optimal point — was a rather tricky task. One could hardly tell if a local minimum found was really a global minimum. The discontinuity came from the reordering of the data points as we change the trial values of the exponents and the critical temperature. As we show in the following, we have eliminated this discontinuity by treating data points for different system size separately.

In what follows, a data point consists of a rescaled estimate y , a rescaled error d and a rescaled parameter x at which y and d are estimated. In the present case, $y = ((\pi/2)\langle W^2 \rangle - 2)\log(L/L_0)$ and $x = (K - K_{KT})(\log(L/L_0))^2$. Therefore, x , y and d depend on trial values for various parameters in general. Here we denote one standard deviation by d . Also we denote the i -th data point for the system size L by $P_{L,i} \equiv (x_{L,i}, y_{L,i}, d_{L,i})$. These data points are ordered so that $x_{L,i} < x_{L,i+1}$. In the previous estimator, we dealt with all the data points without regard to the system size. Therefore, the order of the data points may change as the trial values for the exponents vary. Here we have no such reordering due to the change in the trial values.

For each system size L' , we connect adjacent points $P_{L',i}$ and $P_{L',i+1}$ by a straight line. Then, for each combination of a data point $P_{L,i}$ and a system size L' , we choose j such that $x_{L',j} < x_{L,i} < x_{L',j+1}$. Next, we consider a point at $x = x_{L,i}$ on the line that connects two points, $P_{L',j}$ and $P_{L',j+1}$. We denote this point by $P_{L,i}^{L'}$. Since the value $y_{L,i}^{L'}$ is expressed as a linear combination of $y_{L',j}$ and $y_{L',j+1}$,

$$y_{L,i}^{L'} \equiv py_{L',j} + qy_{L',j+1}, \quad (A.1)$$

$$p \equiv \frac{x_{L',j+1} - x_{L,i}}{x_{L',j+1} - x_{L',j}}, \quad q \equiv 1 - p, \quad (A.2)$$

the error $d_{L,i}^{L'}$, which comes from errors $d_{L',j}$ and $d_{L',j+1}$, can be estimated through the ordinary error propagation rule. To be specific,

$$d_{L,i}^{L'} = \sqrt{p^2 d_{L',j}^2 + q^2 d_{L',j+1}^2}. \quad (A.3)$$

For convenience, we define $P_{L,i}^{L'} \equiv P_{L,i}$. In an ideal case where the linear approximation is good and the statistical and systematic errors are negligible, all $P_{L,i}^{L'}$'s for various L' should coincide with each other.

Here we assume that the linear approximation is good and the systematic errors are negligible while the statistical errors are not necessarily negligible. In order to evaluate the coincidence, then, we consider the weighted

sum of deviations of the points $P_{L,i}^{L'}$, i.e.,

$$S_{L,i} \equiv \sum_{L'} \frac{1}{n-1} \left(\frac{y_{L,i}^{L'} - \bar{y}_{L,i}}{d_{L,i}^{L'}} \right)^2 \quad (\text{A.4})$$

with

$$\bar{y}_{L,i} \equiv \sum_{L'} \frac{y_{L,i}^{L'}}{\sum_{L'} \frac{1}{d_{L,i}^{L'}}^2}, \quad (\text{A.5})$$

where n is the number of distinct system sizes. As statistics tells, the expectation value of $S_{L,i}$ is 1. When we define S as the sum of all $S_{L,i}$'s, it evaluates quality of the finite-size-scaling plot. Its expectation value equals the number of data points N . The acceptable range of parameters is determined by

$$S < \min S + m, \quad (\text{A.6})$$

where m is of order $O(1)$.

Table I. The $v(G_p)$ and $a(G_p)$ for $S = 1/2$ quantum XY model.

G_p	$v(G_p)$	$a(G_p)$
1	$\frac{1}{2}(e^{-\frac{\Delta\tau}{2}J} + 1)$	$-\frac{1}{4}J$
2	$\frac{1}{2}(e^{\frac{\Delta\tau}{2}J} - 1)$	$\frac{1}{4}J$
3	$\frac{1}{2}(1 - e^{-\frac{\Delta\tau}{2}J})$	$\frac{1}{4}J$

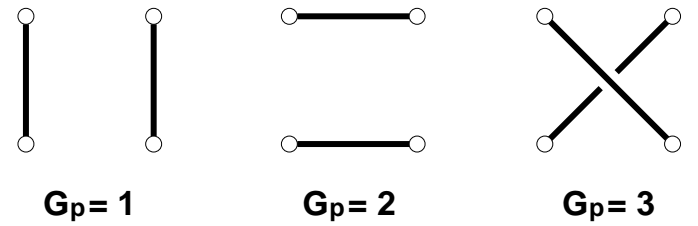
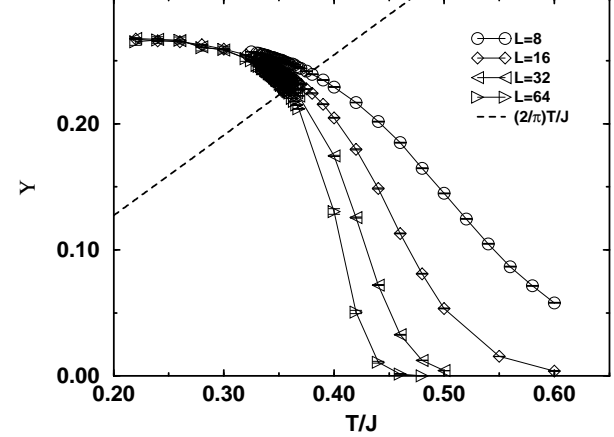
- [1] H.-Q. Ding and M. S. Makivić: Phys. Rev. B **42** (1990) 6827.
- [2] M. S. Makivić and H.-Q. Ding: Phys. Rev. B **43** (1991) 3562.
- [3] H.-Q. Ding: Phys. Rev. B **45** (1992) 230.
- [4] J. M. Kosterlitz and D. J. Thouless: J. Phys. C **6** (1973) 1181.
- [5] J. Sznajd: Phys. Rev. B **45** (1992) 489.
- [6] H.-Q. Ding and M. S. Makivić: Phys. Rev. B **45** (1992) 491.
- [7] R. Gupta, J. DeLapp, G. G. Batrouni, G. C. Fox, C. F. Baillie and J. Apostolakis: Phys. Rev. Lett. **61** (1988) 1996.
- [8] R. Gupta and C. F. Baillie: Phys. Rev. B **45** (1992) 2883.
- [9] J. Sólyom and T. A. L. Ziman: Phys. Rev. B **30** (1984) 3980.
- [10] H. Weber and P. Minnhagen: Phys. Rev. B **37** (1987) 5986.
- [11] J. M. Kosterlitz: J. Phys. C **7** (1974) 1046.
- [12] P. Olsson: Phys. Rev. B **52** (1995) 4526.
- [13] D. R. Nelson and J. M. Kosterlitz: Phys. Rev. Lett. **39** (1977) 1201.
- [14] See for example, *Quantum Monte Carlo Methods in Equilibrium and Nonequilibrium Systems*, ed. M. Suzuki, (Springer Verlag, Heidelberg, 1987).
- [15] E. L. Pollock and D. M. Ceperley: Phys. Rev. B **36** (1987) 8343.
- [16] M. S. Makivić: Phys. Rev. B **46** (1992) 3167.
- [17] H. G. Evertz, M. Marcu and G. Lana: Phys. Rev. Lett. **70** (1993) 875.
- [18] N. Kawashima: J. Stat. Phys. **82** (1996) 131.
- [19] N. Kawashima and J. E. Gubernatis: J. Stat. Phys. **80** (1995) 169.
- [20] B. B. Beard and U.-J. Wiese: Phys. Rev. Lett. **77** (1996) 5130.
- [21] K. Harada and N. Kawashima: Phys. Rev. B **55** (1997) R11949.
- [22] H. Mino: Comp. Phys. Comm. **66** (1991) 25.
- [23] N. Kawashima and N. Ito: J. Phys. Soc. Jpn. **62** (1993) 435.

Table II. The squared winding number $\langle \mathbf{W}^2 \rangle$.

T/J	$L = 8$	$L = 16$	$L = 32$	$L = 64$
0.220		2.429(3)	2.433(6)	2.41(2)
0.240		2.214(3)	2.225(5)	2.22(2)
0.260		2.040(3)	2.046(5)	2.05(2)
0.280		1.876(2)	1.865(4)	1.86(2)
0.300		1.728(2)	1.722(4)	1.73(2)
0.320		1.592(2)		1.57(1)
0.325	1.582(1)	1.557(2)	1.540(3)	1.538(5)
0.330	1.552(1)	1.524(2)	1.508(3)	1.493(3)
0.332	1.542(1)	1.510(2)	1.492(3)	1.478(3)
0.334	1.528(1)	1.492(2)	1.478(3)	1.471(3)
0.335	1.521(1)	1.489(2)	1.471(2)	1.454(3)
0.336	1.518(1)	1.483(1)	1.463(2)	1.450(2)
0.337	1.508(1)	1.475(1)	1.455(2)	1.446(2)
0.338	1.505(1)	1.466(1)	1.444(2)	1.433(2)
0.339	1.500(1)	1.4617(9)	1.442(1)	1.425(1)
0.340	1.491(1)	1.4556(9)	1.434(1)	1.418(1)
0.341	1.486(1)	1.4480(9)	1.426(1)	1.407(1)
0.342	1.480(1)	1.4417(9)	1.419(1)	1.400(1)
0.343	1.4727(9)	1.4374(9)	1.409(1)	1.392(1)
0.344	1.4682(9)	1.4292(8)	1.403(1)	1.385(1)
0.345	1.4633(9)	1.4214(9)	1.396(1)	1.377(1)
0.346	1.4571(9)	1.4149(9)	1.388(1)	1.366(1)
0.347	1.451(1)	1.408(1)	1.384(2)	1.359(2)
0.348	1.445(1)	1.401(1)	1.370(2)	1.348(2)
0.349	1.439(1)	1.396(1)	1.365(2)	1.342(2)
0.350	1.433(1)	1.391(1)	1.356(2)	1.334(2)
0.351	1.426(1)	1.379(2)	1.348(2)	1.319(2)
0.352	1.423(1)	1.376(1)	1.338(2)	1.309(2)
0.353	1.417(1)	1.369(1)	1.337(2)	1.308(2)
0.354	1.412(1)	1.360(1)	1.327(2)	1.298(3)
0.355	1.403(1)	1.354(2)	1.322(2)	1.286(3)
0.356	1.395(2)	1.349(2)	1.311(2)	1.280(5)
0.357	1.393(2)	1.336(2)	1.302(2)	1.270(5)
0.358	1.386(2)	1.336(2)	1.298(2)	1.262(5)
0.359	1.380(2)	1.330(2)	1.284(2)	1.255(5)
0.360	1.373(1)	1.322(2)	1.279(2)	1.247(4)
0.362	1.368(2)	1.305(3)	1.260(2)	1.21(1)
0.364	1.356(2)	1.296(2)	1.246(2)	1.20(1)
0.366	1.340(2)	1.280(2)	1.227(2)	1.18(2)
0.368	1.328(2)	1.262(2)	1.207(2)	1.14(1)
0.370	1.318(2)	1.249(2)		
0.375	1.290(2)	1.214(2)		
0.380	1.259(1)	1.180(2)		
0.390	1.203(1)	1.105(2)		
0.400	1.146(1)	1.024(2)	0.872(2)	0.65(1)
0.420	1.033(1)	0.856(2)	0.598(2)	0.242(6)
0.440	0.917(1)	0.676(2)	0.328(2)	0.050(3)
0.460	0.804(1)	0.492(2)	0.142(1)	0.007(1)
0.480	0.686(1)	0.338(2)	0.0518(7)	0.0008(3)
0.500	0.579(1)	0.214(1)	0.0171(4)	
0.520	0.479(1)			
0.540	0.388(1)			
0.550		0.0564(6)		
0.560	0.310(1)			
0.580	0.2465(9)			
0.600	0.1935(9)	0.0132(3)		

Table II. The squared winding number $\langle \mathbf{W}^2 \rangle$ (continued).

T/J	$L = 12$	$L = 24$	$L = 48$	$L = 96$	$L = 128$
0.339	1.475(1)	1.449(1)	1.432(1)	1.416(1)	1.416(1)
0.340	1.468(1)	1.442(1)	1.423(1)	1.411(1)	1.409(1)
0.341	1.462(1)	1.432(1)	1.414(1)	1.401(1)	1.398(1)
0.342	1.4557(9)	1.426(1)	1.409(1)	1.392(1)	1.389(1)
0.343	1.449(1)	1.417(1)	1.397(1)	1.382(1)	1.379(1)
0.344	1.443(1)	1.412(1)	1.392(1)	1.375(1)	1.370(1)
0.345	1.4368(9)	1.404(1)	1.383(1)	1.366(1)	1.363(1)
0.346	1.4295(9)	1.398(1)	1.374(1)	1.357(1)	1.350(1)

Fig. 1. Three types of graphs for $S = 1/2$ quantum XY model.Fig. 2. Helicity modulus (or super fluid density) $\Upsilon = (T/2)\langle \mathbf{W}^2 \rangle$ as a function of temperature. The universal jump is expected at the point where $\Upsilon = 2T/\pi$. Error bars are drawn but most of them are so small that they cannot be recognized.

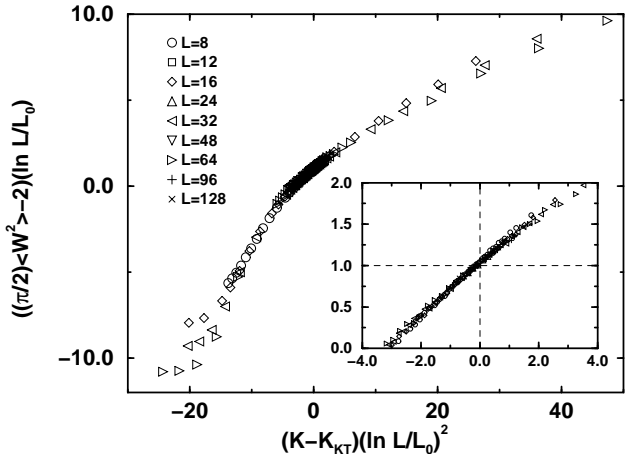


Fig. 3. A rescaled plot of the winding number fluctuation. The inset is an enlarged view near the critical point.

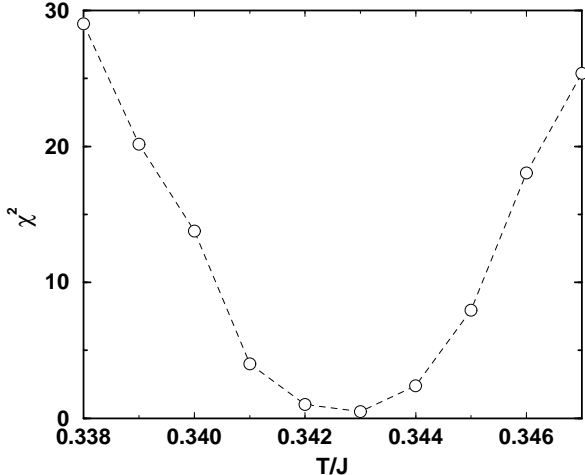


Fig. 5. Chi-square values of the fitting with $A(T)$ fixed to be 1.

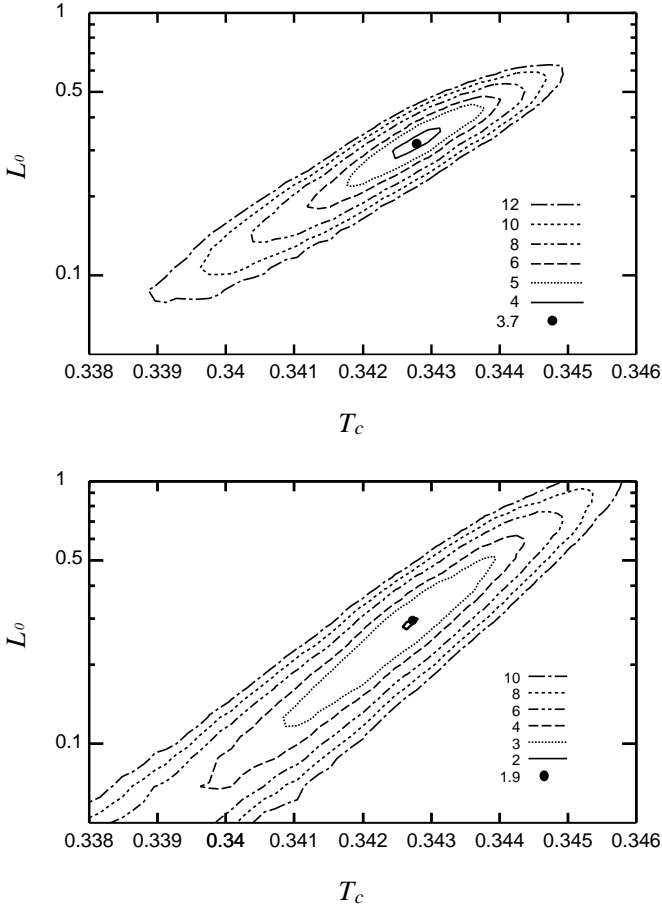


Fig. 4. Contour plots of the cost function for evaluating finite-size-scaling plots. The plotted value is defined as S/N in Appendix. The smallest system size used is $L = 8$ for the top figure and $L = 12$ for the bottom.

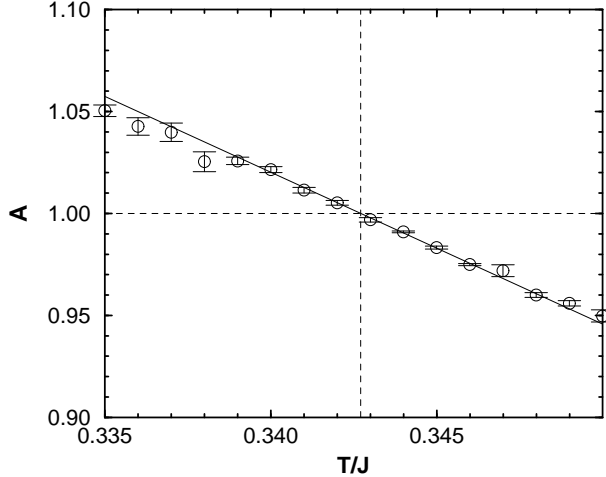


Fig. 6. Helicity modulus divided by the magnitude of its universal jump. The dashed vertical line indicates the critical temperature at which the solid line crosses the dashed horizontal line ($A = 1$). The solid line is determined by a linear fitting.